Research Article Vol. 32, No. 27 / 30 Dec 2024 / Optics Express 48035
Optics EXPRESS

Measurement of inherent optical properties of water based on multiple scattering profiles using underwater off-axis single-photon lidar

ZHENWU WENG,[1,2,†] JIAXIN SUN,[1,2,†] ZHIFENG YANG,[1,2,†] ZHENGQIAN LUO,[3,4] AND MINGJIA SHANGGUAN[1,2,5]

[1]State Key Laboratory of Marine Environmental Science, College of Ocean and Earth Sciences, Xiamen University, Xiamen 361102, China
[2]Key Laboratory of Underwater Acoustic Communication and Marine Information Technology (Xiamen University), Ministry of Education, Xiamen 361102, China
[3]Fujian Key Laboratory of Ultrafast Laser Technology and Applications, Xiamen University, Xiamen 361105, China
[4]zqluo@xmu.edu.cn
[5]mingjia@xmu.edu.cn
[†]These authors contributed equally.

Abstract: Accurately measuring inherent optical properties (IOPs) in water is fundamental for characterizing light transmission in aquatic environments and advancing our understanding of biogeochemical processes. Lidar, with its capability for continuous day-and-night observations and strong water penetration, holds great potential for detecting optical parameters in water. However, ocean lidar faces challenges in addressing ill-posed equations and mitigating the effects of multiple scattering when detecting IOPs. In this study, a method for IOP detection based on multiple scattering profiles is proposed and demonstrated. First, a semi-analytic Monte Carlo approach was applied to analyze the relationship between multiple scattering profiles measured by off-axis lidar and IOPs. Next, a tank experiment was conducted to establish an analytical expression for this relationship. Subsequently, field experiments were carried out in the South China Sea using underwater single-photon lidar. Compared to *in-situ* measurements, the statistical root mean square error values were 0.007 m^{-1} for the scattering coefficient, 0.012 m^{-1} for the beam attenuation coefficient, and 0.014 m^{-1} for the absorption coefficient, validating the feasibility of the proposed method. Overall, this new IOP measurement approach is expected to contribute to advances in ocean biogeochemical cycle research.

1. Introduction

The inherent optical properties (IOPs) of water, including the absorption coefficient (a), scattering coefficient (b), and attenuation coefficient (c), play an important role in various oceanographic assessments [1]. These properties are pivotal for evaluating ocean primary productivity [2], estimating phytoplankton biomass [3], measuring particulate organic carbon (POC) [4], and assessing underwater imaging quality [5]. For instance, the particulate beam attenuation coefficient (c_p) is used to estimate the concentration of particulate organic matter (POC) [6]. Additionally, the absorption coefficient (a) can serve as a proxy for the concentration of dissolved organic material (DOM) [7] and chlorophyll-a concentration (Chl) [8], providing insights into the presence and abundance of these substances in the water.

The measurement of IOPs can generally be classified into two categories: *in-situ* measurement and remote sensing. *In-situ* devices, such as commercial high spectral absorption and attenuation meter (WET Labs ac-s) [9] and LISST-VSF [10], offer high precision and reliability but are limited in coverage and are complex to operate. Remote sensing, on the other hand, provides a broad and rapid acquisition of water body information, serving as an important supplementary

#543467 https://doi.org/10.1364/OE.543467
Journal © 2024 Received 27 Sep 2024; revised 15 Nov 2024; accepted 22 Nov 2024; published 17 Dec 2024

Optics EXPRESS

method for water parameter measurement. Among these, lidar technology has become a key tool for ocean profile remote sensing due to its strong water penetration capability, continuous day-and-night observation, and high depth resolution [11]. It has been widely applied in fields such as scattering layer detection [12,13], Chl profile detection [14], temperature and salinity measurement [15,16], shallow water depth measurement [17], underwater imaging [5], fish monitoring [18–20], and internal wave detection [21,22].

However, lidar still faces several challenges in measuring IOPs of water. Firstly, lidar encounters the issue of ill-posed equation when inverting the lidar attenuation coefficient (K_{lidar}) and the 180° backscattering coefficient ($\beta(\pi)$), where a single equation is insufficient to solve for the two unknowns ($\beta(\pi)$ and K_{lidar}) simultaneously. To address this issue, researchers have proposed various algorithms, including the Collis slope method assuming negligible vertical variation in $\beta(\pi)$ [23], the Klett [24] and Fernald [25] algorithms assuming a specific relationship between $\beta(\pi)$ and K_{lidar}, and the perturbation method [26] assuming minimal vertical variation in K_{lidar}. However, these assumptions introduce some degree of systematic error. Furthermore, to invert these parameters without assuming a relationship between K_{lidar} and $\beta(\pi)$, high-spectral-resolution lidar (HSRL) technology has been developed [27–30]. This technology can simultaneously measure Mie backscattered and Brillouin backscattered signals, allowing two equations to be used to solve for the two unknowns ($\beta(\pi)$ and K_{lidar}). However, even with accurate inversion of $\beta(\pi)$ and K_{lidar}, it is still necessary to establish the relationships between K_{lidar} and IOPs, and between $\beta(\pi)$ and IOPs, to further derive the IOPs of water. For example, to establish the relationship between $\beta(\pi)$ and the backscattering coefficient (b_b), a conversion factor (χ) is required [31]. However, studies show that the χ factor varies significantly [32]. For K_{lidar}, it is typically related to the c or the diffuse attenuation coefficient (K_d) [33].

Additionally, the extensive multiple scattering that occurs during laser transmission in water not only affects the inversion of K_{lidar} and $\beta(\pi)$ in lidar systems but also impacts the relationship between K_{lidar}, $\beta(\pi)$, and water IOPs. For instance, research indicates that when multiple scattering significantly contributes to the backscattered signal, as in the case of the spaceborne ICESat-2 platform, K_{lidar} tends to approximate the K_d. Conversely, when the backscattered signal is predominantly influenced by single scattering, as with underwater lidar, K_{lidar} approximates the c [33]. This indicates that the IOPs of the water determine the distribution of multiple scattering in the lidar backscattered signal, which also implies that the distribution of multiple scattering can be used to infer the IOPs of water.

In previous work, an off-axis lidar system based on single-photon detection technology has been developed to overcome strong near-field signal interference and improve measurement dynamic range. This system has been successfully applied to detect water optical parameters [34–37], underwater oil spills [38], water depth [17], and bubbles [39]. In off-axis underwater lidar systems, within a range of less than 3 m, the geometric overlap factor (Q) is 0, meaning that the lidar receives only multiple scattering profiles. This study will use these profiles to measure IOPs.

The organization of this paper is as follows: First, based on Monte Carlo (MC) simulation methods, the mechanism by which parameters a, b, and c affect multiple scattering profile are investigated, providing a theoretical basis for using off-axis lidar to invert IOPs from multiple scattering profile. Next, an analytical formula for IOPs is established through tank experiments. Furthermore, field experiments are conducted, and the IOPs data obtained from *in-situ* measurements are compared with the results from off-axis lidar measurements to validate the feasibility of the method. Finally, the influence of scattering phase functions on the measurements of b and c was discussed to validate the robustness of the method under different water conditions.

Optics EXPRESS

2. Influence of IOPs on multiple scattering profiles of off-axis lidar

2.1. MC simulation

Due to the multiple scattering that occurs during laser transmission in highly scattering water media, the lidar backscattered signal consists of both single and multiple scattering components. The single-scattering signal only exists when $Q > 0$, while the multiple-scattering signal is present along the entire lidar transmission path. In lidar, the Q refers to the degree of overlap between the field of view (FOV) of the receiving telescope and the laser beam illumination area in space. Figure 1(a) illustrates the distribution of Q for off-axis lidar when only single scattering signals are present. When the detection range is less than R_1, Q is 0, meaning the lidar cannot detect any backscattered signals. As the range increases to R_2, Q gradually increases from 0 to 1. Here, R_1 represents the range at which the Q just becomes non-zero, and R_2 represents the range at which Q just reaches 1. Beyond this point, the laser beam is fully within the FOV of telescope, and Q remains at 1.

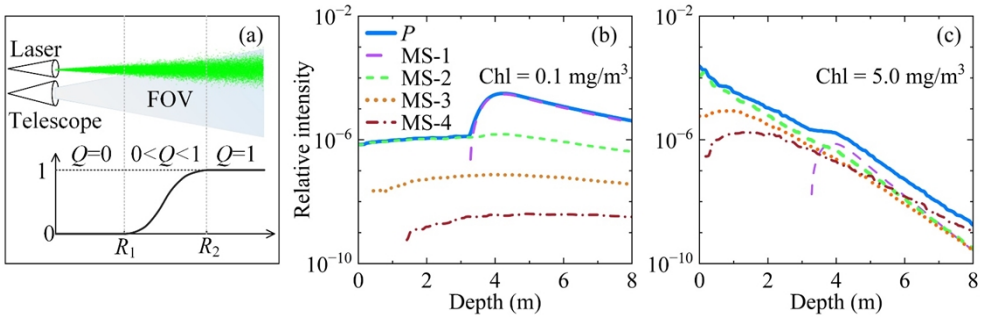

Fig. 1. (a) Schematic diagram of transceiver system of off-axis lidar with Q shown in the bottom; (b) MC simulation signals at Chl of 0.1 mg/m^3, with P representing total signal. MS-n (n = 1, 2, 3) represent the multiple scattering components of P for scattering orders n, while n = 4 represents the sum of signals with scattering orders greater than 3; (c) same as (b) at a higher Chl of 5.0 mg/m^3.

However, when multiple scattering occurs during laser transmission, the distribution of Q will be altered. In the 0 to R_1 range where Q was originally 0 in Fig. 1(a), backscatter profiles can still be detected due to the presence of multiple scattering signals. These profiles, containing only multiple scattering signals, are referred to as the multiple scattering profiles. This multiple scattering profile is governed by the IOPs of the water. To investigate how IOPs affect the multiple scattering profile, this article will utilize MC simulations. The MC simulation is based on statistical principles, which simulates transmission of photons underwater by stochastic sampling, thus effectively reflects multiple scattering in water. This simulation method has been widely used in all kinds of ocean lidar, including spaceborne, airborne, shipborne and underwater lidar system. This study adopted the semi-analytical MC simulation to enhance simulation efficiency [40]. The detailed process of MC simulations can be referenced in previous studies [40,41].

The distribution of backscattered profiles using MC simulations under low and high Chl conditions is shown in Fig. 1(b) and 1(c), respectively. In the simulation, the lidar hardware parameters are based on those of an actual lidar system, as listed in Table 1. The bio-optical model used for calculating the IOPs of water based on Chl references our previous study [42], and the widely used Petzold scattering phase function is adopted [43]. In the Fig. 1, P represents the total lidar signal, and MS-n (n = 1,2,3) represent the multiple scattering signal components of P for scattering orders of n, while MS-4 corresponds to the sum of signals with scattering orders greater than 3. It can be observed from the figures that, whether under low Chl condition

Optics EXPRESS

(Fig. 1(b)) or high Chl condition (Fig. 1(c)), there are no single scattering signals, only multiple scattering signals, in the near-field region from 0 to about 3 m. Moreover, for Chl of 0.1 mg/m^3 (Fig. 1(b)), single scattering remains dominant in the backscattered signal beyond 3 m. In contrast, for Chl of 5 mg/m^3 (Fig. 1(c)), the contribution of multiple scattering signals increases beyond 3 m, and after 5 m, multiple scattering signals surpass single scattering signals. The differences in IOPs lead to variations in the proportion of multiple scattering profile, resulting in changes in the shape of the backscattered signal.

Table 1. Key parameters of off-axis lidar

Parameter	Value
Wavelength	532 nm
Diameter of telescope	2.1 mm
FOV of telescope	10 mrad
Diameter of laser beam	1 mm
Laser divergence angle	1.5 mrad
Distance between telescope and laser beam	15.5 mm
Photon number	10^8

2.2. *Influence of a and b on multiple scattering profiles*

Subsequently, the effects of a, b, and c on the multiple scattering profile is examined separately. Table 2 lists the input values for optical parameters a and b, with a ranging from 0.04 m^{-1} to 1 m^{-1} and b ranging from 0.002 m^{-1} to 2 m^{-1}. There are 700 combinations of a and b, covering conditions from pure water to turbid water. In the case where a is constant and b is varied, the backscattered signals of the off-axis lidar obtained from the MC simulation are shown in Fig. 2(a) and (b). In Fig. 2(a), a is 0.1 m^{-1}, and in Fig. 2(b), a is 1 m^{-1}. Note that the y-axis is logarithmic scale. It is obviously that the near-field signal from 0 to 3 m can be fitted with a linear function. The signal intensity increases with increasing b at both low and high a condition. For near-field signals ranging from 0 to 3 m, a linear function $\ln(P)=K\cdot r+B$ can be used for fitting, where P is the backscattered signal intensity at a detected depth of r, K is the slope of the linear function and B is the intercept. The relationship between B and b, obtained by linearly fitting $\ln(P)$ from Fig. 2(a) and 2(b), is shown in Fig. 2(c). As seen in the figure, b and B follow an exponential distribution. The line represents the exponential fitting results, while the points are derived from fitting the data in Fig. 2(a) and 2(b) using the equation $\ln(P)=K\cdot r+B$.

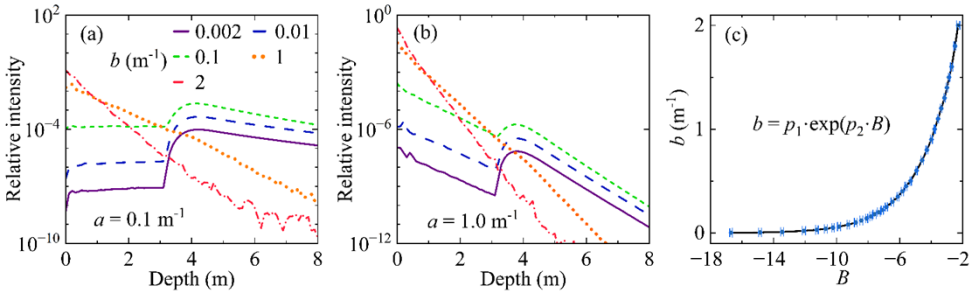

Fig. 2. MC-simulated off-axis lidar backscattered signals with constant a and varying b: (a) $a=0.1$ m^{-1}, b ranging from 0.002 to 2 m^{-1} (b) $a=1.0$ m^{-1}, b ranging from 0.002 to 2 m^{-1}; (c) the relationship between b and B obtained from linear fitting of $\ln(P)$ for signals in (a) and (b).

Optics EXPRESS

Table 2. Values of *a* and *b* for MC simulations

a (m^{-1})	0.04	0.05	0.06	0.07	0.08	0.09	0.10	0.11	0.12	0.13
	0.14	0.15	0.17	0.20	0.25	0.30	0.40	0.50	0.70	1.00
b (m^{-1})	0.002	0.005	0.01	0.02	0.03	0.04	0.05	0.06	0.08	0.10
	0.12	0.14	0.16	0.18	0.20	0.22	0.25	0.30	0.35	0.40
	0.45	0.50	0.60	0.70	0.80	0.90	1.00	1.10	1.20	1.30
	1.40	1.50	1.60	1.80	2.00	—	—	—	—	—

To further verify that B is solely determined by b and is independent of a, the same analysis is conducted with constant b and varying a. The results are shown in Fig. 3. Figure 3 shows the distribution of backscattered signals as a varies from 0.04 m^{-1} to 1 m^{-1} with b set at 0.002 m^{-1}, 0.2 m^{-1}, and 2 m^{-1}, respectively. After processing the data for these three cases, the statistical B values are shown in Table 3. The standard deviation (SD) and coefficient of variation (CV) of B, under varying a but constant b, are also presented. The formulas for calculating SD and CV are as follows:

$$\mathrm{SD} = \sqrt{\frac{\sum_{i=1}^{n} (B_i - \bar{B})^2}{n-1}} \tag{1}$$

$$|\mathrm{CV}| = \frac{S}{|\bar{B}|} \times 100\% \tag{2}$$

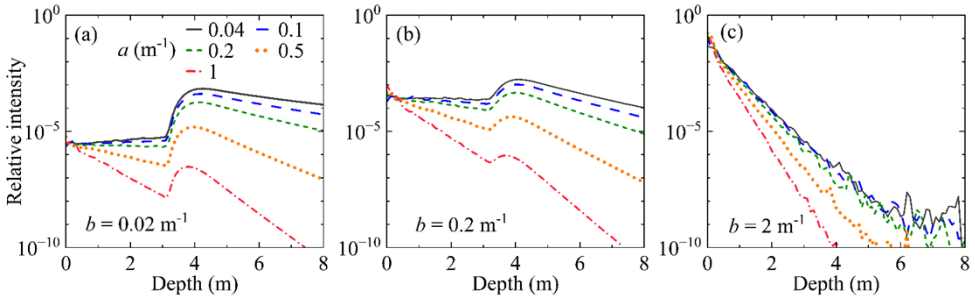

Fig. 3. MC-simulated off-axis lidar backscattered signals with constant b and varying a with (a) $b = 0.02\ m^{-1}$; (b) $b = 0.2\ m^{-1}$ and (c) $b = 2\ m^{-1}$.

Table 3. Statistical results of *B* with varying *a* under constant *b*

b (m^{-1})	a (m^{-1})					$\bar{B}$	SD	$\lvert CV \rvert$
	0.04	0.1	0.2	0.5	1			
0.02	−12.134	−12.158	−12.124	−11.891	−11.819	−12.025	0.054	0.5%
0.2	−7.377	−7.371	−7.360	−7.315	−7.176	−7.320	0.029	0.4%
2	−2.307	−2.136	−2.363	−2.110	−2.133	−2.210	0.040	1.8%

Optics EXPRESS

where $\bar{B}$ is the mean of B at constant b, and n is the number of gradients of a. Table 3 shows that neither the SD nor the CV coefficient is affected by a, indicating that B is independent of a. Furthermore, B is solely related to b and follows an exponential relationship with b.

2.3. Influence of c on multiple scattering profiles

To investigate how parameter c affects multiple scattering backscattered signals, MC simulations are conducted with c set to 0.5 and 2 m^{-1}, and a varied from 0.1 to 1 m^{-1}. The backscattered signals are shown in Fig. 4(a) and 4(b), respectively. It can be seen from the figures that when c remains constant, the slope of the ln(P) profile remains essentially unchanged. Table 4 lists the parameters for MC simulation under the same c and different a. By fitting the multiple scattering profiles from 0-3 m with ln(P)=$K\cdot r + B$ and analyzing the relationship between K and c, as shown in Fig. 4(c), it is evident that K is uniquely determined by c. Changes in a (i.e., changes in b) do not affect K, and there is a linear relationship between c and K. The linear fit of c versus K is shown as the line in Fig. 4(c), with a high fitting accuracy and an R-squared (R^2) value of 0.99. From the above analysis, it can be concluded that for the 0-3 m near-field signals of off-axis lidar, when the subsurface water is vertically homogeneous, the signal ln(P) can be represented by a linear function. In this function, b determines the intercept B, while c determines the slope K. Moreover, the relationship between b and B follows an exponential distribution, while the relationship between c and K follows a linear distribution, that is:

$$\begin{cases} b = p_1 \cdot \exp(p_2 \cdot B) \\ c = p_3 \cdot K + p_4 \end{cases} \tag{3}$$

where p_1, p_2, p_3, and p_4 are fitting parameters, which will be determined through subsequent tank experiments. The reason for adopting experimental determination rather than MC simulation for these parameters is the presence of certain discrepancies between the laser divergence angle and FOV of the telescope incorporated into the MC, and the actual lidar system. Moreover, parameter B is related to intensity and can only be determined through experiments conducted at specific laser intensity levels.

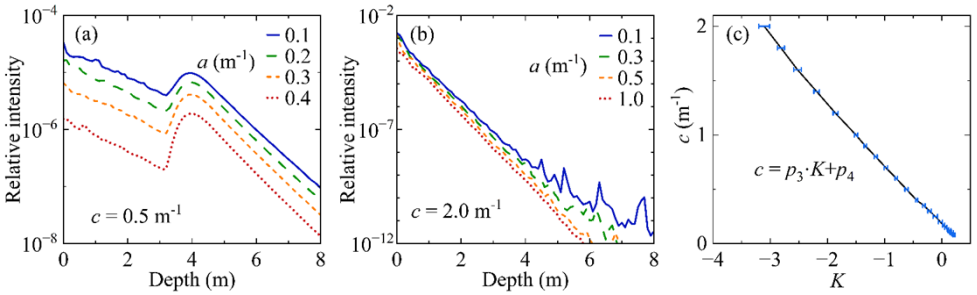

Fig. 4. (a) MC simulation signals at constant c and varying a with (a) $c = 0.5\ m^{-1}$ and (b) $c = 2.0\ m^{-1}$; (c) statistic results of K using MC case 2 simulation signals.

Optics EXPRESS

Table 4. Values of *c* and *a* for MC Simulation

c (m^{-1})	a (m^{-1})												
0.08	0.04	0.05	0.06	0.07		—	—	—	—	—	—	—	—
0.09	0.04	0.05	0.06	0.07	0.08	—	—	—	—	—	—	—	—
0.10	0.04	0.05	0.06	0.07	0.08	—	—	—	—	—	—	—	—
0.11	0.04	0.05	0.06	0.07	0.08	0.09	0.1	—	—	—	—	—	—
0.12	0.04	0.05	0.06	0.07	0.08	0.09	0.1	—	—	—	—	—	—
0.13	0.04	0.05	0.06	0.07	0.08	0.09	0.1	—	—	—	—	—	—
0.15	0.04	0.05	0.06	0.07	0.08	0.09	0.1	—	—	—	—	—	—
0.17	0.04	0.05	0.06	0.07	0.08	0.09	0.1	—	—	—	—	—	—
0.20	0.04	0.05	0.06	0.07	0.08	0.09	0.1	—	—	—	—	—	—
0.25	0.04	0.05	0.06	0.07	0.08	0.09	0.1	—	—	—	—	—	—
0.30	0.04	0.05	0.06	0.07	0.08	0.09	0.1	—	—	—	—	—	—
0.35	0.04	0.05	0.06	0.07	0.08	0.09	0.1	—	—	—	—	—	—
0.4	0.04	0.05	0.06	0.07	0.08	0.09	0.1	—	—	—	—	—	—
0.5	0.04	0.05	0.06	0.07	0.09	0.1	0.11	0.12	0.13	0.14	0.15	0.17	0.2
0.6	0.04	0.05	0.06	0.07	0.09	0.1	0.11	0.12	0.13	0.14	0.15	0.17	0.2
0.7	0.04	0.05	0.06	0.07	0.09	0.1	0.11	0.12	0.13	0.14	0.15	0.17	0.2
0.8	0.04	0.05	0.06	0.07	0.09	0.1	0.11	0.12	0.13	0.14	0.15	0.17	0.2
0.9	0.04	0.05	0.06	0.07	0.09	0.1	0.11	0.12	0.13	0.14	0.15	0.17	0.2
1.0	0.04	0.05	0.06	0.07	0.09	0.1	0.11	0.12	0.13	0.14	0.15	0.17	0.2
1.2	0.04	0.05	0.06	0.07	0.09	0.1	0.11	0.12	0.13	0.14	0.15	0.17	0.2
	0.3	0.4	0.5	—	—	—	—	—	—	—	—	—	—
1.4	0.04	0.05	0.06	0.07	0.09	0.1	0.11	0.12	0.13	0.14	0.15	0.17	0.2
	0.3	0.4	0.5	—	—	—	—	—	—	—	—	—	—
1.6	0.04	0.05	0.06	0.07	0.09	0.1	0.11	0.12	0.13	0.14	0.15	0.17	0.2
	0.3	0.4	0.5	—	—	—	—	—	—	—	—	—	—
1.8	0.04	0.05	0.06	0.07	0.09	0.1	0.11	0.12	0.13	0.14	0.15	0.17	0.2
	0.3	0.4	0.5	—	—	—	—	—	—	—	—	—	—
2.0	0.04	0.05	0.06	0.07	0.09	0.1	0.11	0.12	0.13	0.14	0.15	0.17	0.2
	0.3	0.4	0.5	—	—	—	—	—	—	—	—	—	—

3. Tank experiment

To overcome the interference at the air-sea interface and to facilitate the deployment of lidar on underwater platforms such as autonomous underwater vehicles (AUVs) and remotely operated vehicles (ROVs), an underwater lidar has been adopted. Detailed hardware specifications can be found in previous work by our group [37], and a brief introduction of the system is provided here. The system uses a 532 nm pulsed laser with a pulse width of 501 ps and a repetition rate of 1 MHz. The lidar adopts an off-axis configuration. The receiver uses a fiber-coupled small-aperture collimator with a 10.9 mm focal length, and the backscattered signal is detected by a silicon avalanche photodiode (Si-APD). The lidar has dimensions of 20 cm in diameter and 40 cm in length, an average power consumption of approximately 80 W, and a weight of 15 kg. Due to the watertight design of the entire lidar system, it can be deployed at depths of up to 1 km underwater, where the pressure is approximately 10 MPa.

Optics EXPRESS

To determine the values of p_1, p_2, p_3, and p_4 in Eq. (3), the lidar was first tested in an experimental water tank. Figure 5 illustrates the top-down view of the experimental tank layout, which includes the underwater lidar system and a high spectral absorption and attenuation meter (WET Labs ac-s) for measuring the a and the c. The dimensions of the tank are 14 m × 2 m × 1 m (length × width × depth). To minimize the reflection of the laser off the inner walls, a black coating was applied to the interior surfaces of the tank. In the experiment, the ac-s was placed at a position 2 m away from the lidar, as shown in the schematic diagram of Fig. 5. Both the lidar and the ac-s were positioned horizontally at a depth of approximately 0.5 m.

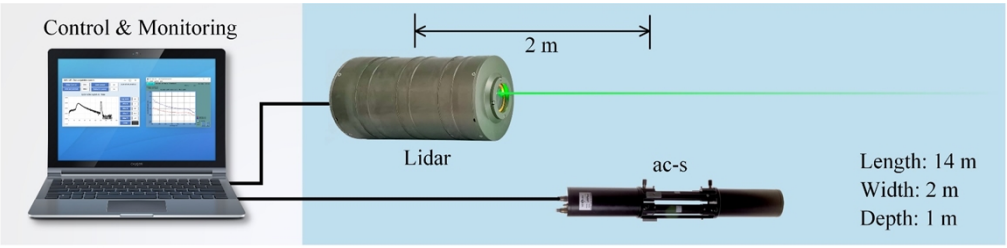

Fig. 5. Schematic diagram of the tank experiment.

During the experiment, tap water was first added to the tank, and then lake water was added to alter the IOPs of the water. The lake water was sourced from a natural lake at Xiamen University's Xiang'an campus (24.61°N, 118.31°E), with a value of c of approximately 6.0 m^{-1}. To gradually change the IOPs, the lake water was first diluted, and then the diluted lake water was uniformly sprayed into the tank using a sprayer. After slowly stirring to ensure uniform distribution, lidar and ac-s measurements were conducted. Additionally, the water temperature in the tank was recorded every five minutes using a thermometer for subsequent calibration of the a measured by the ac-s. Since both the tank water and lake water are fresh water, the salinity of the tank water is considered to be 0‰. The calibration methods for the ac-s, as well as the correction methods for temperature and salinity, and the scattering error correction method for the absorption coefficient, followed the protocols in Refs. [44,45]. After correction, the absorption coefficient and attenuation coefficient of pure water (a_w and c_w) were added to the ac-s measurements to generate the total absorption coefficient (a) and total attenuation coefficient (c) at 532 nm, with a_w at 532 nm being 0.043 m^{-1} and c_w being 0.045 m^{-1} [46,47]. The calibration and correction methods for ac-s were also applied in subsequent field experiments.

The results from 29 sets of data measured using the above methods are shown in Fig. 6. Figure 6(a) displays the lidar backscattered signals at different c values, with different colored lines corresponding to the various c values measured by ac-s. The peaks at approximately 13 m are attributed to wall reflection. During the addition of lake water, the a increased from 0.09 m^{-1} to 0.32 m^{-1}, and the c increased from 0.15 m^{-1} to 1.43 m^{-1}. The effective detection distance of the lidar in the water decreased from over 12 m (blue line, limited by the tank size) to less than 3 m (red line). It can be observed from the figure that as c increases, the slope and intensity of the near-field multiple scattering profile also gradually increase. By statistically analyzing the slope K and intercept B of ln(P) within the near field (0-3 m) and fitting the K to c and the B to b using Eq. (3), the parameters p_1, p_2, p_3, and p_4 in Eq. (3) were determined, with R^2 values exceeding 0.99. Finally, Eq. (3) was updated to:

$$\begin{cases} b = 0.003 \cdot \exp(0.592 \cdot B) \\ c = -0.574 \cdot K + 0.126 \end{cases} \tag{4}$$

Optics EXPRESS

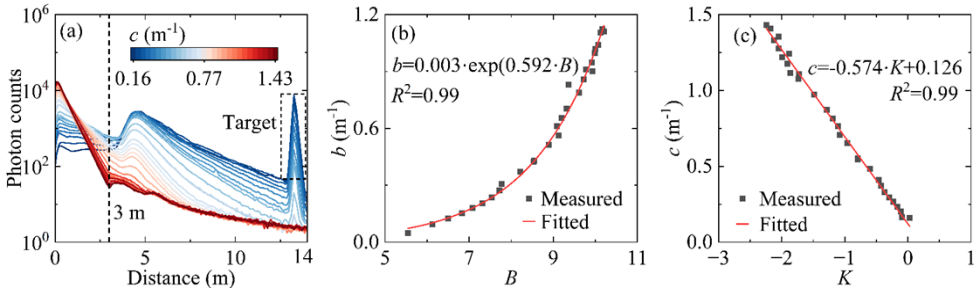

Fig. 6. (a) Lidar backscattered signals at different c values measured by ac-s; (b) exponential relationship between b and B, with dots representing measured data and the line representing the fitted result; (c) linear relationship between c and K, with dots representing measured data and the line representing the fitted result.

Finally, analytical formulas for retrieving the water's b and c were established based on the multiple scattering profile, and a can be determined by c minus b.

4. Field experiment

To validate the feasibility and effectiveness of retrieving water IOPs based on multiple scattering profiles, a field experiment was conducted from May 16 to 24, 2024, aboard the Zhong Haike 777 Research Vessel in the South China Sea. The lidar was mounted on a long steel tube on the side of the aft deck and placed vertically into the water, as shown in Fig. 7(a). The lidar's outlet was positioned approximately 1.5 m below the ocean surface, effectively suppressing solar background noise while minimizing the impact of surface bubbles on the measurements. The laser pulse energy was set to the same value as in the tank experiment, approximately 200 nJ. The experiment was conducted at 12 stations in the South China Sea, and Fig. 7(b) shows the locations of these stations, with the background representing the monthly averaged Chl for May 2024, derived from the moderate resolution imaging spectroradiometer (MODIS). The coordinates of these stations are listed in Table 5, with all stations having a Chl of less than 0.17 mg/m^3. Among them, stations S5 to S8 were located close to each other and near an island reef where the Chl was significantly higher than in the surrounding areas. During the measurements at these stations, within the first hour of the vessel's arrival, the WET Labs ac-s was used to measure the a and c, and the Seabird SBE-25 CTD was used for simultaneous temperature and salinity measurements.

Table 5. Station location information.

Station	Longitude (°E)	Latitude (°N)	Station	Longitude (°E)	Latitude (°N)
S1	110.389	17.996	S7	111.493	17.113
S2	110.687	17.837	S8	111.493	17.113
S3	110.646	17.710	S9	111.680	18.106
S4	111.081	17.331	S10	111.132	17.986
S5	111.482	17.109	S11	111.123	17.350
S6	111.488	17.107	S12	110.735	17.830

Figure 8 shows the depth profiles of the lidar backscattered signals at each station, with different stations separated by white narrow bars. The black dashed line indicates the depth of 4.5 m. Since the lidar's outlet is positioned 1.5 m below the water surface, the lidar data begins collecting from a depth of 1.5 m. From Fig. 8, it can be observed that the residence times at

Optics EXPRESS

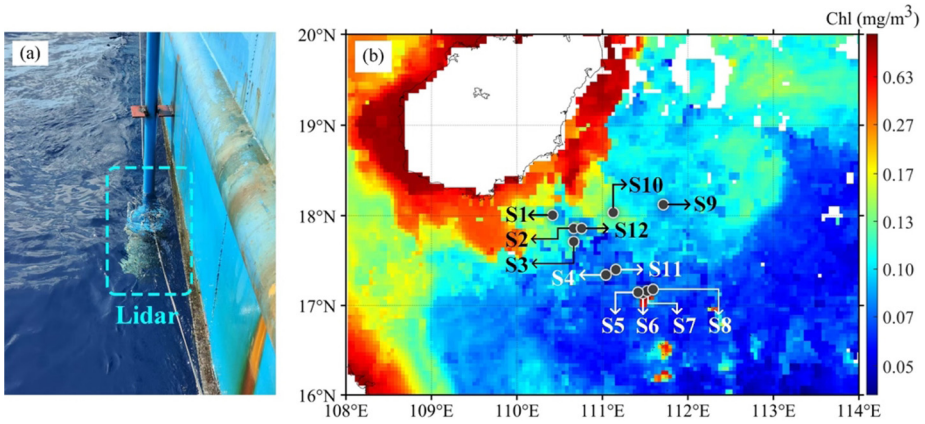

Fig. 7. (a) Schematic diagram of the fixed lidar on the research vessel, with the laser outlet positioned 1.5 m below the surface; (b) Location map of the 12 experimental stations, with the background showing the monthly averaged Chl for May 2024 obtained from MODIS.

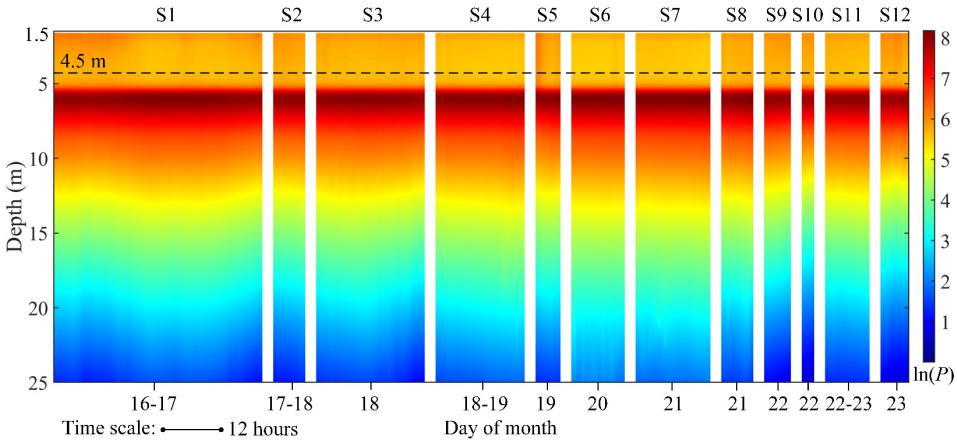

Fig. 8. Profiles measured by lidar at the 12 stations.

each station vary, with S1 having a residence time of nearly 20 hours, which allows for further analysis of the diurnal changes of IOPs in the subsurface. In this study, the near-field signals, namely the multiple scattering profiles ranging from 1.5 to 4.5 m, were used for further retrieval of IOPs. After removing the background light, the near-field signal was fitted using the linear function $\ln(P) = K \cdot r + B$, and the obtained K and B were substituted into Eq. (4) to retrieve c and b. Subsequently, coefficient a was calculated by c minus b.

The retrieved IOPs of these stations are shown in Fig. 9, where the lines and pentagrams represent the IOPs measured by the lidar and ac-s, respectively. The horizontal position of the pentagrams corresponds to the first half-hour after the vessel's arrival at each station, as the ac-s measurements were conducted within the first hour post-arrival. Except for station S1 in the first subplot of Fig. 9, the IOPs at each station varied slowly over time. Notably, all three optical parameters (a, b and c) at S1 decreased over time, reaching minimum values around 4:00 AM on May 17, before beginning to increase at 6:00. These trends can also be observed from the lidar-measured profiles of S1 in Fig. 8, where the penetrating depth is greater in the central period of S1, indicating cleaner surface water at night.

Optics EXPRESS

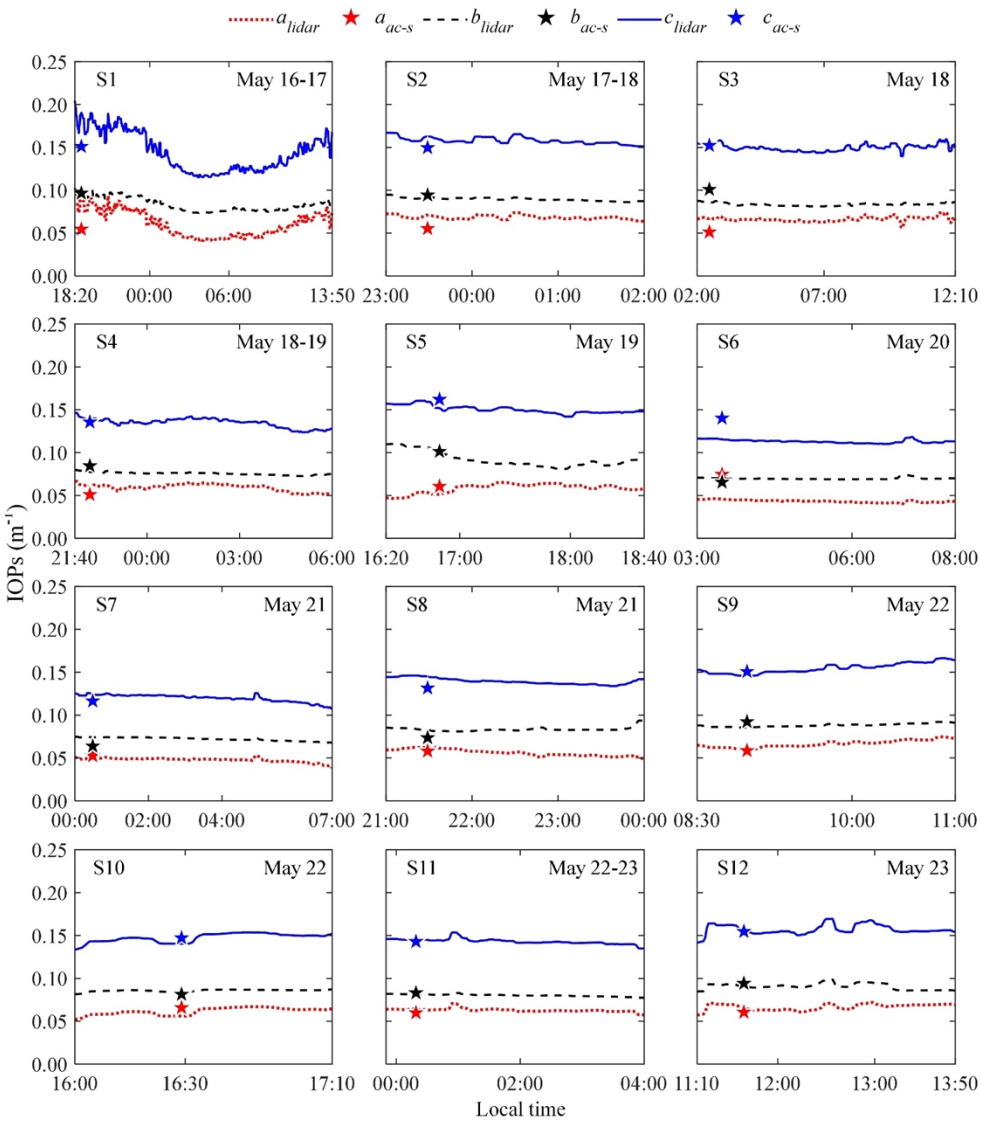

Fig. 9. IOPs observed by lidar at the 12 stations, with lines and pentagrams representing the values measured by lidar and ac-s, respectively.

To compare the lidar and ac-s measurements, the IOPs retrieved by the lidar during the first hour at each station were averaged to contrast with the measurements of ac-s at 3 m. Figure 10 presents the comparison of the IOPs measured by the lidar with those measured by ac-s at each station. It can be seen that the variation ranges of both b and c are small across these stations, but the values measured by the lidar for both b and c show a consistent trend with those measured by ac-s. However, since a is derived by subtracting b from c, and both parameters have measurement errors, this results in a larger discrepancy between the lidar-derived a and the ac-s measurements. For example, the lidar-measured c value at S1 exceeds that of ac-s by about 0.03 m^{-1}, leading to an overestimation of a, while the lidar underestimated c at S6, causing an underestimate of a. Nevertheless, as shown in Fig. 10(b), the root mean square error (RMSE) values for b, c, and a

Optics EXPRESS

are 0.007 m^{-1}, 0.012 m^{-1}, and 0.014 m^{-1}, respectively, demonstrating the applicability of the IOPs retrieval method.

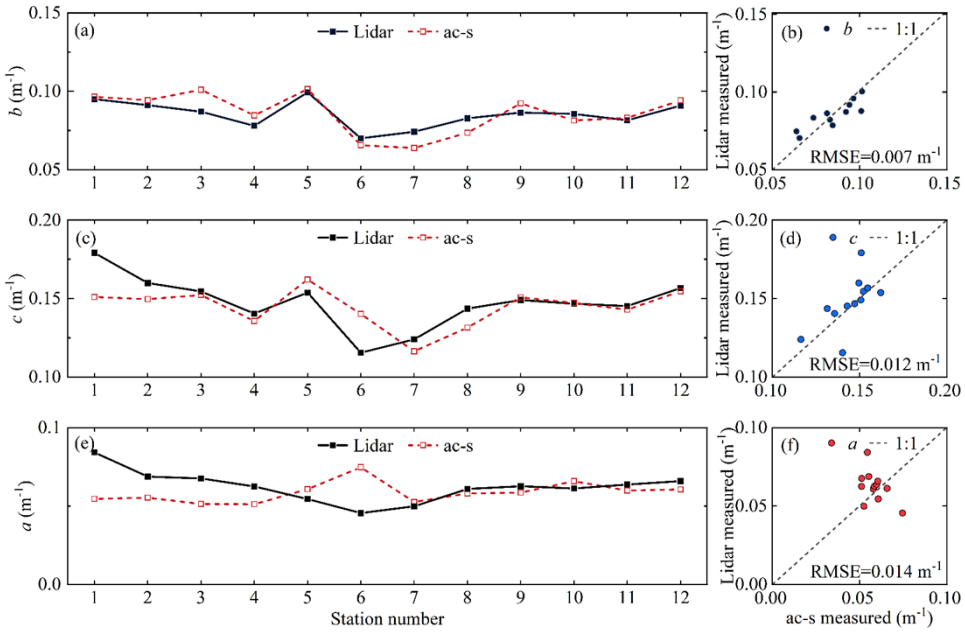

Fig. 10. Comparison of lidar and ac-s measured IOPs at a depth of 3 m. Left column shows IOPs varying with station, while right directly contrast these two techniques.

5. Discussion

To demonstrate the applicability of the proposed method in different oceanic environments, including the effects of varying scattering phase functions (SPFs) and different particle abundances on the measurements, MC simulations were conducted using different particle SPFs according to [48]. Specifically, the six phase functions, including Petzold average SPF (Petzold), Petzold flat-back SPF (Flat-back), Fournier-Forand SPF (FF), One-Term Henyey-Greenstein SPF (OTHG), Two-Term Henyey-Greenstein SPF (TTHG), and Ad Hoc SPF (Ad hoc), span the range of functional forms seen in the oceanography literature [48]. As shown in Fig. 11, the adopted SPFs exhibit significant differences from one another. In addition to particle scattering, water molecules also contribute to photon scattering, and their contribution can be more significant in clear ocean environments. The total scattering phase function of water, considering the SPFs of both water molecules and particles, can be expressed as [49]:

$$\tilde{\beta}(\theta) = \eta \cdot \tilde{\beta}_w(\theta) + (1 - \eta) \cdot \tilde{\beta}_p(\theta) \tag{5}$$

where η is the ratio of the scattering coefficient of water (b_w) to the total scattering coefficient (b), $\tilde{\beta}_w$is the water SPF [50] and $\tilde{\beta}_p(\theta)$is the particle SPF.

Using six different particle SPFs and the MC simulation and statistical methods described in Section 2, the relationships between b and B, as well as c and K, were derived, as shown in Fig. 12. To facilitate analysis, the mean absolute deviation (MAD) is employed to evaluate the performance of b and c, expressed as follows:

Optics EXPRESS

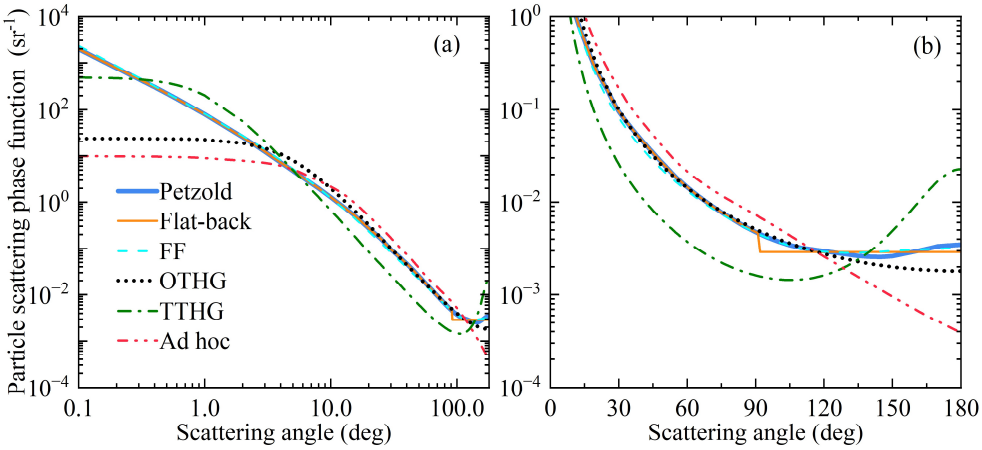

Fig. 11. Phase functions used in the MC simulations: (a) scattering angles in logarithmic scale, (b) scattering angles in linear scale.

$$\mathrm{MAD} = \frac{1}{6}\sum_{i=1}^{6}|X_i - \overline{X}| \tag{6}$$

where x_i is the inversed b or c of the i-th SPF, is the average of x_i. Additionally, the mean relative error (MRE) is calculated to further evaluate b, expressed as follows:

$$\mathrm{MRE} = \frac{1}{6}\sum_{i=1}^{6}\frac{|X_i - \overline{X}|}{\overline{X}} \tag{7}$$

As shown in Fig. 12(a) and (b), the relationship between b and B varies under different SPFs. Specifically, when the value of b ranges from 0 to approximately 2.2 m^{-1}, although the MRE remains below 30%, the MAD is relatively large, ranging from 0 m^{-1} to about 0.6 m^{-1}. From Fig. 12(a), the most significant deviation is observed for the TTHG SPF, which is likely attributed to its lower scattering intensity within the intermediate angle range. Regarding the relationship between c and K, as shown in Fig. 12(c), The relationship between c and K is generally linear, with consistent slopes across the six SPFs, although the intercepts vary. This results in the MAD of the retrieved c remaining nearly constant at approximately 0.1 m^{-1} within the range of 0 m^{-1} to 2.5 m^{-1}. When c is less than 0.2 m^{-1}, the deviation can reach around 50%, whereas for c greater than 0.4 m^{-1}, the deviation decreases to below 30%. This indicates that the proposed method may be more applicable to coastal waters. Additionally, as shown in Fig. 12(c), the results based on the OTHG and Ad hoc SPFs differ significantly from those of the other SPFs. The OTHG SPF, initially proposed by Henyey and Greenstein [51] for describing the scattering of interstellar dust, requires further validation to determine its suitability for characterizing the scattering properties of ocean particles. The Ad hoc SPF, on the other hand, is an artificially defined extreme case relative to the TTHG, but its physical significance appears limited compared to measurement results [49]. Excluding these two SPFs from the analysis reduces the MAD of c to less than 0.03 m^{-1}. Overall, the relationships between b and B, as well as c and K, depend to some extent on the particle SPF. Therefore, when applying the methods in this work to retrieve c and b, prior knowledge of the particle SPF can significantly improve retrieval accuracy.

Optics EXPRESS

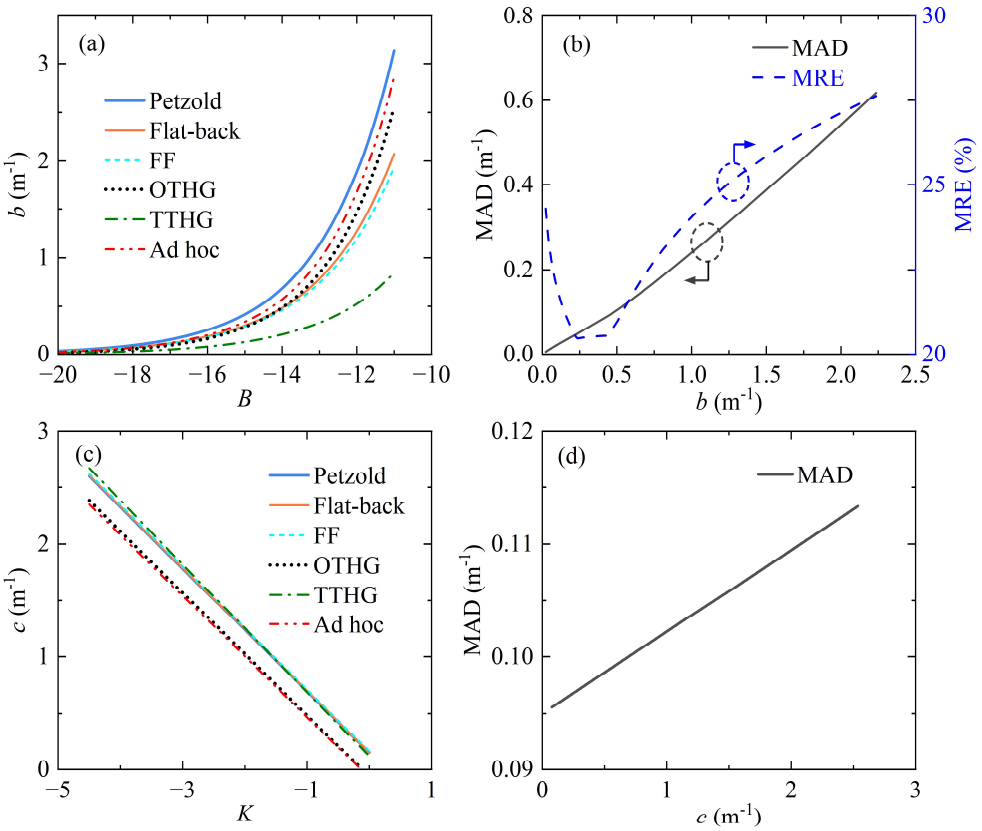

Fig. 12. Results under six SPFs: (a) b vs B; (b) MAD and MRE of b; (c) c vs K; (d) MAD of c.

6. Conclusion

This study proposes and validates a new method for deriving the IOPs of water using the multiple scattering profile from an underwater off-axis single-photon lidar. To the best of our knowledge, this is the first time that multiple scattering profile have been used to simultaneously measure the optical properties a, b, and c.

In this study, the MC method was applied, utilizing the control variable approach to explore the effects of a, b, and c on the near-field multiple scattering profile of the underwater off-axis single-photon lidar. Subsequently, the slope K and intercept B of the ln(P) of the multiple scattering profiles were used to invert parameters c and b. Moreover, water tank experiments were conducted to establish the quantitative relationships between K and c, as well as B and b. Finally, field experiments were carried out in the South China Sea, where the RMSE for b, c, and a measured by the lidar and the ac-s were found to be 0.007 m^{-1}, 0.012 m^{-1}, and 0.014 m^{-1}, respectively, demonstrating the feasibility of this method.

However, this study could only obtain the IOPs near the outlet of the lidar, which somewhat limited the profiling capability of ocean lidar. Therefore, future work will focus on deriving the vertical profiles of IOPs using more multiple scattering profiles. Additionally, the tank experiment, due to its limited size, may still be affected by signals reflected from the tank walls, despite them being painted black. Moreover, tap water was used in the experiment, which differs from seawater in terms of salinity, organic and inorganic particles, and other factors. The

Optics EXPRESS

impact of these factors on the measurements will be analyzed in future work. Furthermore, changes in lidar system parameters necessitate re-establishing the relationships between b and B, and c and K. Specifically, variations in the emitted laser wavelength affect the absorption and scattering coefficients of water, while factors such as the telescope aperture, emission angle, and relative positions of the optics influence the Q. These factors alter the measured distance and corresponding relationships. Therefore, systematic calibration and relationship establishment, as outlined in this paper, are essential when applying this method to measure c and b in water. Finally, the underwater lidar will be integrated into AUVs, allowing lidar observations to extend from shallow waters to the deep ocean, thus unleashing the full potential of lidar in ocean observations, particularly in deep-sea environments.

Funding. National Natural Science Foundation of China (42476184); National Key Research and Development Program of China (2022YFB3901704); Fundamental Research Funds for the Central Universities (20720200107); Joint Funds of the National Natural Science Foundation of China (U2106210).

Disclosures. The authors declare no conflicts of interest.

Data availability. The data that support the findings of this study are available from the corresponding author upon reasonable request.

References

1. A. H. Barnard, W. S. Pegau, J. R. V. Zaneveld, *et al.*, "Global relationships of the inherent optical properties of the oceans," J. Geophys. Res. **103**(C11), 24955–24968 (1998).
2. M. Behrenfeld, E. Boss, D. A. Siegel, *et al.*, "Carbon-based ocean productivity and phytoplankton physiology from space," Global Biogeochem. Cycles **19**(1), 1 (2005).
3. M. Galí, M. Falls, H. Claustre, *et al.*, "Bridging the gaps between particulate backscattering measurements and modeled particulate organic carbon in the ocean," Biogeosciences **19**(4), 1245–1275 (2022).
4. D. Stramski, R. A. Reynolds, M. Babin, *et al.*, "Relationships between the surface concentration of particulate organic carbon and optical properties in the eastern South Pacific and eastern Atlantic Oceans," Biogeosciences **5**(1), 171–201 (2008).
5. A. Maccarone, K. Drummond, A. McCarthy, *et al.*, "Submerged single-photon LiDAR imaging sensor used for real-time 3D scene reconstruction in scattering underwater environments," Opt. Express **31**(10), 16690–16708 (2023).
6. W. Cui, D. Wang, F. Gong, *et al.*, "The vertical distribution of the beam attenuation coefficient and its correlation to the particulate organic carbon in the north South China Sea," in *Remote Sensing of the Ocean, Sea Ice, Coastal Waters, and Large Water Regions 2016*, (SPIE, 2016), 280–292.
7. M. S. Twardowski and P. L. Donaghay, "Photobleaching of aquatic dissolved materials: Absorption removal, spectral alteration, and their interrelationship," J. Geophys. Res.: Oceans **107**(C8), 6 (2002).
8. A. Morel and S. Maritorena, "Bio-optical properties of oceanic waters: A reappraisal," J. Geophys. Res.: Oceans **106**(C4), 7163–7180 (2001).
9. G. Neukermans, H. Loisel, X. Mériaux, *et al.*, "In situ variability of mass-specific beam attenuation and backscattering of marine particles with respect to particle size, density, and composition," Limnol. Oceanogr. **57**(1), 124–144 (2012).
10. H. Sandven, A. S. Kristoffersen, Y.-C. Chen, *et al.*, "In situ measurements of the volume scattering function with LISST-VSF and LISST-200X in extreme environments: evaluation of instrument calibration and validity," Opt. Express **28**(25), 37373–37396 (2020).
11. C. Jamet, A. Ibrahim, Z. Ahmad, *et al.*, "Going beyond standard ocean color observations: lidar and polarimetry," Front. Mar. Sci. **6**, 251 (2019).
12. F. E. Hoge, C. W. Wright, W. B. Krabill, *et al.*, "Airborne lidar detection of subsurface oceanic scattering layers," Appl. Opt. **27**(19), 3969–3977 (1988).
13. O. A. Bukin, A. Yu. Major, A. N. Pavlov, *et al.*, "Measurement of the lightscattering layers structure and detection of the dynamic processes in the upper ocean layer by shipborne lidar," Int. J. Remote Sens. **19**(4), 707–715 (1998).
14. P. Chen, C. Jamet, D. Liu, *et al.*, "Lidar remote sensing for vertical distribution of seawater optical properties and chlorophyll-a from the East China Sea to the South China Sea," IEEE Trans. Geosci. Remote Sensing **60**, 1–21 (2022).
15. Y. Zhao, Y. Wang, K. Liang, *et al.*, "Underwater temperature and salinity measurement by Rayleigh–Brillouin spectroscopy using Fizeau interferometer and PMT array," Remote Sens. **16**(12), 2214 (2024).
16. Y. Wang, J. Zhang, Y. Zheng, *et al.*, "Brillouin scattering spectrum for liquid detection and applications in oceanography," Opto-Electron. Adv. **6**(1), 220016 (2023).
17. M. Shangguan, Z. Weng, Z. Lin, *et al.*, "Day and night continuous high-resolution shallow-water depth detection with single-photon underwater lidar," Opt. Express **31**(26), 43950 (2023).
18. J. H. Churnside, J. J. Wilson, V. V. Tatarskii, *et al.*, "Airborne lidar for fisheries applications," Opt. Eng. **40**(3), 406–414 (2001).

Optics EXPRESS

19. D. L. Murphree, C. D. Taylor, R. W. McClendon, *et al.*, "Mathematical modeling for the detection of fish by an airborne laser," AIAA J. **12**(12), 1686–1692 (1974).
20. J. L. Squire and H. D. Krumboltz, "Profiling pelagic fish schools using airborne optical lasers and other remote sensing techniques," in (2004).
21. J. H. Churnside and L. A. Ostrovsky, "Lidar observation of a strongly nonlinear internal wave train in the Gulf of Alaska," Int. J. Remote Sens. **26**(1), 167–177 (2005).
22. J. H. Churnside, R. D. Marchbanks, J. H. Lee, *et al.*, "Airborne lidar detection and characterization of internal waves in a shallow Fjord," J. Appl. Remote Sens. **6**(1), 063611 (2012).
23. R. T. H. Collis, "Lidar: A new atmospheric probe," Q. J. R. Meteorol. Soc. **92**(392), 220–230 (1966).
24. J. D. Klett, "Stable analytical inversion solution for processing lidar returns," Appl. Opt. **20**(2), 211–220 (1981).
25. F. G. Fernald, "Analysis of atmospheric lidar observations: some comments," Appl. Opt. **23**(5), 652–653 (1984).
26. J. H. Churnside, J. W. Hair, C. A. Hostetler, *et al.*, "Ocean backscatter profiling using high-spectral-resolution lidar and a perturbation retrieval," Remote Sens. **10**(12), 2003 (2018).
27. B. Gross, C. Hostetler, Y. Hu, *et al.*, "Combined atmospheric and ocean profiling from an airborne high spectral resolution lidar," EPJ Web Conf. 119 (2016).
28. J. A. Schulien, M. J. Behrenfeld, J. W. Hair, *et al.*, "Vertically- resolved phytoplankton carbon and net primary production from a high spectral resolution lidar," Opt. Express **25**(12), 13577 (2017).
29. Y. Zhou, Y. Chen, H. Zhao, *et al.*, "Shipborne oceanic high-spectral-resolution lidar for accurate estimation of seawater depth-resolved optical properties," Light: Sci. Appl. **11**(1), 261 (2022).
30. B. Collister, J. Hair, C. Hostetler, *et al.*, "Assessing the utility of high spectral resolution lidar for measuring particulate backscatter in the ocean and evaluating satellite ocean color retrievals," Remote Sens. Environ. **300**, 113898 (2024).
31. X. Zhang, L. Hu, D. Gray, *et al.*, "Shape of particle backscattering in the North Pacific Ocean: the χ factor," Appl. Opt. **60**(5), 1260–1266 (2021).
32. L. Hu, X. Zhang, Y. Xiong, *et al.*, "Variability of relationship between the volume scattering function at 180° and the backscattering coefficient for aquatic particles," Appl. Opt. **59**(10), C31–C41 (2020).
33. H. Gordon, "Interpretation of airborne oceanic lidar: effects of multiple scattering," Appl. Opt. **21**(16), 2996–3001 (1982).
34. M. Shangguan, Y. Guo, Z. Liao, *et al.*, "Sensing profiles of the volume scattering function at 180° using a single-photon oceanic fluorescence lidar," Opt. Express **31**(24), 40393 (2023).
35. M. Shangguan, Z. Liao, Y. Guo, *et al.*, "Sensing the profile of particulate beam attenuation coefficient through a single-photon oceanic Raman lidar," Opt. Express **31**(16), 25398 (2023).
36. M. Shangguan, Z. Liao, Y. Guo, *et al.*, "Simultaneous sensing profiles of beam attenuation coefficient and volume scattering function at 180° using a single-photon underwater elastic-Raman lidar," Opt. Express **32**(5), 8189 (2024).
37. M. Shangguan, Z. Yang, Z. Lin, *et al.*, "Full-day profiling of a beam attenuation coefficient using a single-photon underwater lidar with a large dynamic measurement range," Opt. Lett. **49**(3), 626 (2024).
38. M. Shangguan, Z. Yang, M. Shangguan, *et al.*, "Remote sensing oil in water with an all-fiber underwater single-photon Raman lidar," Appl. Opt. **62**(19), 5301 (2023).
39. M. Shangguan, Z. Yang, Z. Lin, *et al.*, "Compact long-range single-photon underwater lidar with high spatial–temporal resolution," IEEE Geosci. Remote Sensing Lett. **20**, 1–5 (2023).
40. L. R. Poole, D. D. Venable, J. W. Campbell, *et al.*, "Semianalytic Monte Carlo radiative transfer model for oceanographic lidar systems," Appl. Opt. **20**(20), 3653–3656 (1981).
41. Y. Liao, M. Shangguan, Z. Yang, *et al.*, "GPU-accelerated Monte Carlo simulation for a single-photon underwater lidar," Remote Sens. **15**(21), 5245 (2023).
42. M. Shangguan, Y. Guo, Z. Liao, *et al.*, "Shipborne single-photon fluorescence oceanic lidar: instrumentation and inversion," Opt. Express **32**(6), 10204–10218 (2024).
43. T. J. Petzold, "Volume scattering functions for selected ocean waters," in (1972).
44. W. S. Pegau, D. Gray, J. R. V. Zaneveld, *et al.*, "Absorption and attenuation of visible and near-infrared light in water: dependence on temperature and salinity," Appl. Opt. **36**(24), 6035–6046 (1997).
45. R. Z. Zanfeld, V. Zaneveld, C. Kitchen, *et al.*, "Scattering error correction of reflecting-tube absorption meters," in *Ocean Optics XII*, (SPIE, 1994).
46. J. D. Mason, M. T. Cone, E. S. Fry, *et al.*, "Ultraviolet (250–550 nm) absorption spectrum of pure water," Appl. Opt. **55**(25), 7163 (2016).
47. A. Morel, "Optical properties of pure water and pure sea water," Optical aspects of oceanography, (1974).
48. C. D. Mobley, L.K. Sundman, E. Boss, *et al.*, Phase function effects on oceanic light fields, Appl. Opt., **41**(6), 1035–1050 (2002).
49. A. Morel and B. Gentili, "Diffuse reflectance of oceanic waters: its dependence on Sun angle as influenced by the molecular scattering contribution," Appl. Opt. **30**(30), 4427–4438 (1991).
50. C. Mobley, *Light and Water: Radiative Transfer in Natural Waters* (1994).
51. L. C. Henyey and J. L. Greenstein, "Diffuse radiation in the Galaxy," The Astrophysical Journal **93**, 70–83 (1940).